

Detecting the stochastic gravitational wave background with the TianQin detector

Jun Cheng, En-Kun Li,^{*} Yi-Ming Hu,[†] Zheng-Cheng Liang, Jian-dong Zhang, and Jianwei Mei
MOE Key Laboratory of TianQin Mission, TianQin Research Center for Gravitational Physics & School of Physics and Astronomy, Frontiers Science Center for TianQin, Gravitational Wave Research Center of CNSA, Sun Yat-sen University (Zhuhai Campus), Zhuhai 519082, China

The detection of stochastic gravitational wave background (SGWB) is among the leading scientific goals of the space-borne gravitational wave observatory, which would have significant impact on astrophysics and fundamental physics. In this work, we developed a data analysis software, TQSGWB, which can extract isotropic SGWB using the Bayes analysis method based on the TianQin detector. We find that for the noise cross spectrum, there are imaginary components and they play an important role in breaking the degeneracy of the position noise in the common laser link. When the imaginary corrections are considered, the credible regions of the position noise parameters are reduced by two orders of magnitude. We demonstrate that the parameters of various signals and instrumental noise could be estimated directly in the absence of a Galactic confusion foreground through Markov chain Monte Carlo sampling. With only a three-month observation, we find that TianQin could be able to confidently detect SGWBs with energy density as low as $\Omega_{\text{PL}} = 1.3 \times 10^{-12}$, $\Omega_{\text{Flat}} = 6.0 \times 10^{-12}$, and $\Omega_{\text{SP}} = 9.0 \times 10^{-12}$, for power-law, flat, and single-peak models respectively.

I. INTRODUCTION

Stochastic gravitational wave background (SGWB) [1–3] can be produced by the incoherent superposition of large numbers of independent and unresolved gravitational wave sources. According to the different physical mechanisms and historical epochs that contributed to the SGWB, it could be classified into two major types:

a. Astrophysical origin. This class includes a Galactic foreground contributed from Galactic double white dwarfs (DWDs) [4], and extragalactic backgrounds produced by the inspiral and merger of compact binaries, such as massive black hole binaries (MBHBs) [5], stellar-mass black hole binaries (SBBHs) [6, 7], and extreme mass ratio inspirals (EMRIs) [8, 9].

^{*}Corresponding author: lienk@mail.sysu.edu.cn

[†]Corresponding author: huyiming@sysu.edu.cn

The Galactic foreground is comparable with detector noise, and thus is the most distinctive. The Galactic origin also made it anisotropic. On the other hand, the extragalactic background is generally expected to be spatially homogeneous, Gaussian, stationary, unpolarized, and isotropic. The detection of such SGWB can provide important astrophysical information about the source populations, like the mass distribution of the binary, the merger rate evolution, and even the formation mechanisms [10–12].

b. Cosmological origin. It has been suggested that various processes in the early Universe [13, 14], including inflation [15, 16], first-order phase transition [17–19], and networks of topological defects (e.g., cosmic strings) [20, 21] can contribute to the SGWB.

The cosmological SGWB thus encodes precious information about the early Universe, and the detection of it has the potential to significantly improve our understanding of the processes that shaped the early Universe and particle physics beyond the standard model [22]. For example, one can decipher the energy scale and slope of inflation potential, as well as the initial quantum states during inflation by observing the relic gravitational wave (RGW) [23].

The search for SGWB with current experiments, like Advanced LIGO [24], Advanced Virgo [25], and pulsar timing arrays (PTAs) [26–28] are carried out actively. Meanwhile, relevant investigations with future experiments, like the Einstein telescope (ET) [29], the cosmic explorer (CE) [30, 31], as well as space-borne missions such as laser interferometer space antenna (LISA) [32] and TianQin [33] are also performed. With data accumulated during Advanced LIGO and Advanced Virgo’s first observing run (O1) till the third observing run (O3), no observational evidence for SGWB has been reported officially from the LIGO Scientific Collaboration, the Virgo Collaboration and the KAGRA Collaboration (LVK), which places an upper limit on the dimensionless energy density $\Omega_{\text{gw}} \leq 5.8 \times 10^{-9}$ for a frequency-independent (flat) SGWB [34]. Recently, the NANOGrav Collaboration reported an interesting common-spectrum process that can not be easily explained by noise, yet no strong support of quadrupolar spatial correlations can be concluded [35]. Such observations have been later confirmed by PPTA [36] and EPTA [37]. Many hypotheses have been proposed to explain the observed common-spectrum process, including cosmic strings, dark phase transitions, or scalar transverse polarization mode [38–46]. But more observation is needed to draw definitive conclusions.

Since the statistical property of the SGWB is indistinguishable from the instrumental noise, it is challenging to identify SGWB with one interferometer, unless the strength is comparable or even larger than the instrumental noise, as in the case of the Galactic foreground. In principle, one can use the cross-correlation method to identify the existence of SGWB with multiple detectors, using

the fact that SGWB recorded by multiple detectors are correlated, while noise in different detectors are statistically independent [1, 47–50]. For the special case of a triangular-shaped gravitational wave (GW) detector, one can construct a signal-insensitive data stream, also known as the *null channel*, which has been suggested that can play the role of a noise monitoring channel, and can be further used to search for SGWB [51, 52]. The validity of such method had been established through the analysis on the mock LISA data challenge [53, 54].

Many interesting works have emerged for more realistic and robust studies of SGWB. For example, [55] proposed a search method based on principal component analysis (PCA), so that no *a priori* assumption of SGWB spectral shape is needed. Other spectrum-agnostic methods have also been developed [56–58]. Methods like adaptive Markov Chain Monte Carlo (MCMC) have been proposed to identify multicomponent backgrounds [59, 60]. And advances have been made to identify the anisotropy of SGWB [61–64].

In this paper we focus on the mHz frequency band and developed a search method for SGWB with space-borne GW missions like TianQin [33, 65, 66], which we call TQSGWB. We study the detection capability of TianQin to SGWB in the absence of Galactic confusion foreground. We find that the imaginary part of the noise cross spectrum, which was mostly overlooked in the field, can break the degeneracy of position noise in common laser link. We demonstrated the detection capability of TianQin for three representative SGWB spectra, as well as its detection limits.

This paper is organized as follows. In Sec. II we introduce the fundamentals of the SGWB and the three representative spectra. In Sec. III, we describe in detail the noise model of the TianQin detector and its response function. In Sec. IV, we show how one could simulate the data stream by using the power spectral density of SGWB and noise, and also briefly describe the Bayesian analysis technique, as well as our main results. We finally draw our conclusions and discuss possible extensions of this work in Sec. V.

II. FUNDAMENTALS OF STOCHASTIC GRAVITATIONAL-WAVE BACKGROUND

In the transverse-traceless gauge, the metric perturbations $h_{ij}(t, \vec{x})$ corresponding to SGWB can be written as a superposition of plane waves having frequency f and propagating in the direction of \hat{k} ,

$$h_{ij}(t, \vec{x}) = \int_{-\infty}^{\infty} df \int_{S^2} d\hat{k} h_{ij}(f, \hat{k}) e^{i2\pi f(t - \hat{k} \cdot \vec{x}/c)}, \quad (1)$$

where $h_{ij}(f, \hat{k}) = \sum_P h_P(f, \hat{k}) e_{ij}^P(\hat{k})$, $P = \{+, \times\}$ denotes polarization states, and e_{ij}^P are the polarization tensors.

Considering a Gaussian, stationary, unpolarized, spatially homogenous, and isotropic SGWB, the statistical properties of the corresponding Fourier components satisfy [1, 2]

$$\langle h_P(f, \hat{k}) \rangle = 0, \quad (2)$$

$$\langle h_P(f, \hat{k}) h_{P'}^*(f', \hat{k}') \rangle = \frac{1}{16\pi} S_h(f) \delta(f - f') \delta_{PP'} \delta^2(\hat{k}, \hat{k}'), \quad (3)$$

where $\langle \dots \rangle$ denotes the ensemble average, and $S_h(f)$ is the one-sided power spectral density (PSD), which is related to the fractional energy density spectrum $\Omega_{\text{gw}}(f)$ of SGWB as

$$S_h(f) = \frac{3H_0^2}{2\pi^3} \frac{\Omega_{\text{gw}}(f)}{f^3} \text{ and } \Omega_{\text{gw}}(f) = \frac{1}{\rho_c} \frac{d\rho_{\text{gw}}}{d \ln f}. \quad (4)$$

Here, ρ_{gw} is the GWs energy density, $\rho_c = 3H_0^2/(8\pi G)$ represents the critical density, and H_0 is the Hubble constant, for which we assume a fiducial value of $H_0 = 67 \text{ km s}^{-1} \text{ Mpc}^{-1}$ throughout this work [67].

We consider three scenarios as follows: SGWB from the compact binary coalescences (CBCs) (power-law), a scale-invariant inflationary SGWB (flat), and a single-peak spectrum (Gaussian-bump).

- Power-law spectrum

CBCs are among the most promising GW sources for the mHz frequency band [6, 65, 68]. Based on the numerous observations from current ground-based GW detectors [69–73], preliminary studies reveals that CBC can form detectable SGWB for TianQin [74]. The analytic model describing the CBCs background depends on redshift and merger rates [75, 76], whereas the energy of the inspirals can be described by a power-law (PL) spectrum [76–78]

$$\Omega_{\text{CBCs}}(f) = \Omega_{\text{PL}} \left(\frac{f}{f_{\text{ref}}} \right)^{2/3}, \quad (5)$$

where Ω_{PL} denotes the amplitude level at reference frequency f_{ref} . We inject a power-law SGWB with a fiducial value of amplitude $\Omega_{\text{PL}} = 4.4 \times 10^{-12}$ and $f_{\text{ref}} = 3 \text{ mHz}$ [79, 80].

- Flat spectrum

The slow-roll inflation can produce a cosmological-originated SGWB through the amplification of vacuum fluctuations [81–84]. The spectrum and amplitude of such signals strongly depend on the fluctuation power spectrum developed during the early inflationary period.

In the TianQin detection frequency regime, the inflationary background is expected to be scale invariant (flat)

$$\Omega_{\text{Inflation}}(f) = \Omega_{\text{Flat}}. \quad (6)$$

And we choose $\Omega_{\text{Flat}} = 1.0 \times 10^{-11}$ as the fiducial value.

- Gaussian-bump spectrum

Many physical mechanisms in the very early Universe can produce SGWB with a spectrum peak around certain frequencies, including nonperturbative effects during postinflationary preheating, strong first-order phase transitions during the thermal era of the Universe [18, 85–89], or merging of primordial black holes (PBHs) during the early Universe [18, 19]. In the following analysis, we consider a phenomenological spectrum of a Gaussian-bump (or single-peaked) model [90, 91],

$$\Omega_{\text{Bump}} = \Omega_{\text{SP}} \exp \left\{ - \frac{[\log_{10}(f/f_{\text{ref}})]^2}{\Delta^2} \right\}, \quad (7)$$

and we adopt $\Omega_{\text{SP}} = 1.0 \times 10^{-11}$, $\Delta = 0.2$, $f_{\text{ref}} = 3$ mHz as the input parameters [57, 58].

We remind the readers that the Galactic foreground from the DWDs can be dominating in certain frequency range. However, some assumptions adopted in our following analysis do not hold for the Galactic foreground (as it is anisotropic and strong). Therefore we concentrate on the background alone, and will leave the more realistic analysis of both the Galactic foreground and isotropic backgrounds in the future.

III. PRINCIPALS FOR SGWB DETECTIONS WITH TIANQIN

Throughout this work, we consider TianQin as our fiducial detector. It has been proposed that the successful operation of TianQin can reveal great amount of exciting science, such as the origin and evolution of black holes and multi black hole systems [5], the astrophysics of compact binaries[6], the surroundings and nature of black holes[9, 92], the nature of the gravity [93], the expansion of the Universe [94, 95], and so on [66, 74]. The TianQin mission will be composed with three drag-free satellites, forming an equilateral triangle constellation orbiting the Earth with an orbital radius of about 10^5 km, and it adopts a three months on and three months off (3+3) operational model [96, 97].

A. Noise model

Laser links will be established between TianQin satellites, and the detection of GW signal is implemented through laser interferometry. Let us consider the laser link from satellite i to satellite j : the time series of the recorded laser phase $\Phi_{ij}(t)$ are composed with contributions from possible GW signals $\psi_{ij}(t)$ and noise, while the noise can be further classified into laser frequency noise C , position noise n^p , and acceleration noise \vec{n}^a :

$$\begin{aligned}\Phi_{ij}(t) = & C_i(t - L_{ij}/c) - C_j(t) + \psi_{ij}(t) + n_{ij}^p(t) \\ & - \hat{r}_{ij} \cdot [\vec{n}_{ij}^a(t) - \vec{n}_{ji}^a(t - L_{ij}/c)].\end{aligned}\quad (8)$$

Here \hat{r}_{ij} is the unit vector from satellite i pointing to satellite j , L_{ij} is the arm-length between satellite i and j , c is the light speed. The GW strain is given by

$$\psi_{ij}(t) = \frac{h(f, t - L/c, \vec{x}_i) : (\hat{r}_{ij} \otimes \hat{r}_{ij}) \mathcal{T}(f, \hat{r}_{ij} \cdot \hat{k})}{2L}, \quad (9)$$

where $\mathcal{T}(f, \hat{r}_{ij} \cdot \hat{k})$ is the *transfer function* of the interferometer to the GWs for each arm [98–101].

The laser frequency noise $C(t)$ is usually several orders of magnitude higher than other noise. If left untreated, the laser frequency noise will dominate the data and make GW impossible. To suppress the laser frequency noise, the time delay interferometry (TDI) technique [51, 102–105] has been proposed and applied in the analyzing of space-borne GW detections. The principle of TDI is to combine multiple time-shifted laser links into equivalent equal-arm interferometer to cancel the laser frequency noise. Depending on the complexity of the considered satellite motion, the TDI combinations for a Michelson interferometer can be classified into different generations; TDI generation 1.0 assumes a static configuration, TDI generation 1.5 considered a rigid but rotating constellation, and TDI generation 2.0 takes the constant changing of arm-length into account [105, 106]. In this work, we concentrate on TDI generation 1.5 for our analysis.

With the output phases from six different links, it is possible to built three virtual equal arm channels which are called channel X , Y , and Z . We illustrate the Michelson type variable of X channel with the TDI generation 1.5 as [53]

$$\begin{aligned}X(t) = & [\Phi_{12}(t - 3L/c) + \Phi_{21}(t - 2L/c) \\ & + \Phi_{13}(t - L/c) + \Phi_{31}(t)] \\ & - [\Phi_{13}(t - 3L/c) + \Phi_{31}(t - 2L/c) \\ & + \Phi_{12}(t - L/c) + \Phi_{21}(t)].\end{aligned}\quad (10)$$

The Fourier transform of the TDI variable $X(f)$ is

$$\begin{aligned} X_a(f) &= 4i \sin u e^{-2iu} [(n_{31}^a + n_{21}^a) \cos u - (n_{12}^a + n_{13}^a)], \\ X_p(f) &= 2i \sin u e^{-2iu} [(n_{31}^p - n_{21}^p) e^{iu} + (n_{13}^p - n_{12}^p)]. \end{aligned} \quad (11)$$

Here $u = f/f_*$, and $f_* = c/(2\pi L)$ is the characteristic frequency. The others TDI variables Y and Z , can be obtained by cyclic permutation of indices: $1 \rightarrow 2 \rightarrow 3 \rightarrow 1$ in Eqs. (11).

Under the assumption that the position and acceleration noise for all the arms are identical and uncorrelated, three orthogonal TDI channels A , E , and T could be constructed [104, 105, 107],

$$A = \frac{Z - X}{\sqrt{2}}, \quad E = \frac{X - 2Y + Z}{\sqrt{6}}, \quad T = \frac{X + Y + Z}{\sqrt{3}}. \quad (12)$$

The A and E channels are sensitive to GW signals, can has similar properties to Michelson channels, but the T channel is signal insensitive under the low-frequency approximation (or long-wavelength limit), and is also referred to as the *null channel* or noise monitoring channel. The noise power spectral density (PSD) of each channel can than be analytically expressed as [58]

$$\begin{aligned} \langle N_{AA^*} \rangle &= \langle N_{EE^*} \rangle = 8 \sin^2 u \left\{ [2 + \cos u] S^p \right. \\ &\quad \left. + 4[1 + \cos u + \cos^2 u] S^a \right\}, \\ \langle N_{TT^*} \rangle &= 32 \sin^2 u \sin^2 \left(\frac{u}{2} \right) \left\{ S^p + 2[1 - \cos u] S^a \right\}. \end{aligned} \quad (13)$$

Here, $S_{ij}^a(f) = S^a(f) = \langle \bar{n}_{ij}^a(f) \bar{n}_{ij}^{a*}(f) \rangle$, and $S_{ij}^p = S^p(f) = \langle n_{ij}^p(f) n_{ij}^{p*}(f) \rangle$ are nominal spectral density of acceleration noise and position noise respectively,

$$\begin{aligned} S^p(f) &= N^p \frac{\text{m}^2}{\text{Hz}} \left(\frac{1}{2L} \right)^2, \\ S^a(f) &= N^a \frac{\text{m}^2}{\text{s}^4 \text{Hz}} \left(1 + \frac{0.1 \text{mHz}}{f} \right) \left(\frac{1}{2\pi f} \right)^4 \left(\frac{1}{2L} \right)^2, \end{aligned} \quad (14)$$

where $N^p = 1.0 \times 10^{-24}$ and $N^a = 1.0 \times 10^{-30}$ are the noise amplitude parameters. These TianQin noise PSDs are shown in Fig. 1. With the cancellation of laser frequency noise, the acceleration noise dominates the noise at low frequencies, while position noise dominates at high frequencies.

Upon this point, we have adopted an important assumption, that noises from different arms are identical, $S_{ij}^a = S^a$, and $S_{ij}^p = S^p$, naturally the cross spcctrum components $\langle N_{AE^*} \rangle$ will vanish. However, if we account for the differences between different arms, then one must account for the cross spcctral components. The details of all the components of the cross spcctrum matrix are

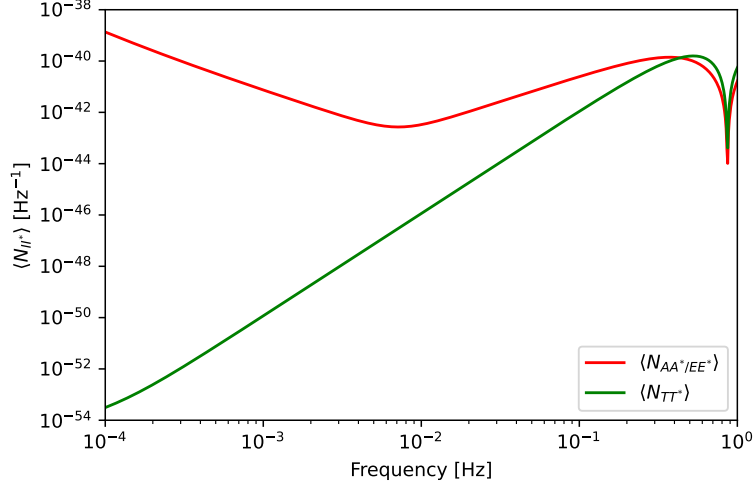


FIG. 1: The noise auto-power spectral density of TianQin in the different channels.

shown in the Appendix A. It is worth emphasizing that the position noise contributions have imaginary components, which mainly comes from e^{iu} in the second term of Eqs. (11), for example,

$$\begin{aligned} \langle N_{AE^*}^p \rangle = \frac{2 \sin^2 u}{\sqrt{3}} \left\{ [1 + 2 \cos u] (S_{23}^p + S_{32}^p - S_{12}^p - S_{21}^p) \right. \\ \left. + i2 \sin u (S_{12}^p - S_{21}^p - S_{13}^p + S_{31}^p + S_{23}^p - S_{32}^p) \right\}. \end{aligned} \quad (15)$$

From Eqs. (A2) and (15), one can observe that the sums of the position and acceleration noise contributions in each arm of the interferometer, e.g., $S_{13}^{a,p} + S_{31}^{a,p}$, always appear together in the autocorrelation PSDs and the real part of some cross spectra components. On the other hand, the differences of the position noise contributions in each arm appear only in the imaginary part of the cross spectra, e.g., $S_{12}^p - S_{21}^p$. This suggests that if only the real components are considered, then certain parameters are degenerate, like S_{12}^p and S_{21}^p . However, the consideration of the imaginary component can break such degeneracy. Thus, one can expect that the constraints on the position noise parameters will be better than the acceleration noise parameters.

B. Response function

In general, the output of each channel in an interferometer consists of the instrumental noise and the signal, which can be expressed in the frequency domain as

$$d_I(f) = n_I(f) + h_I(f), \quad I = \{A, E, T\}. \quad (16)$$

Here, $n(f)$ is the instrumental noise, and $h(f)$ represents the interferometric response to the SGWB

$$h(f) = \sum_P \int_{S^2} d\hat{k} h_P(f, \hat{k}) F^P(f, \hat{k}) e^{-i2\pi f \hat{k} \cdot \vec{x}/c}, \quad (17)$$

with antenna pattern function $F^P(f, \hat{k})$. We can express the auto- and cross spectra of stationary noise and signal as

$$\langle n_I(f) n_J^*(f') \rangle = \frac{1}{2} \delta(f - f') \langle N_{IJ^*} \rangle, \quad (18)$$

$$\langle h_I(f) h_J^*(f') \rangle = \frac{1}{2} \delta(f - f') R_{IJ^*}(f) S_h(f), \quad (19)$$

where $R_{IJ^*}(f)$ is the overlap reduction function [108],

$$R_{IJ^*}(f) = \frac{1}{8\pi} \sum_P \int_{S^2} d\hat{k} F_I^P(f, \hat{k}) F_J^{P*}(f, \hat{k}) e^{-i2\pi f \hat{k} \cdot (\vec{x}_I - \vec{x}_J)}. \quad (20)$$

In the equal arm-length limit, all of the overlap reduction functions $R_{AE^*}(f)$, $R_{AT^*}(f)$, and $R_{ET^*}(f)$ are zero, that is, A , E , and T channels have uncorrelated responses to an isotropic and unpolarized SGWB [2, 53]. As for the average response function $R_{II^*}(f)$, semianalytical expressions [109–112] or numerical methods [113, 114] were usually used. Recently, a fully analytical expression of Michelson type TDI combinations has been derived [115–119], which provides a convenient way to calculate the response, and is adopted in this paper.

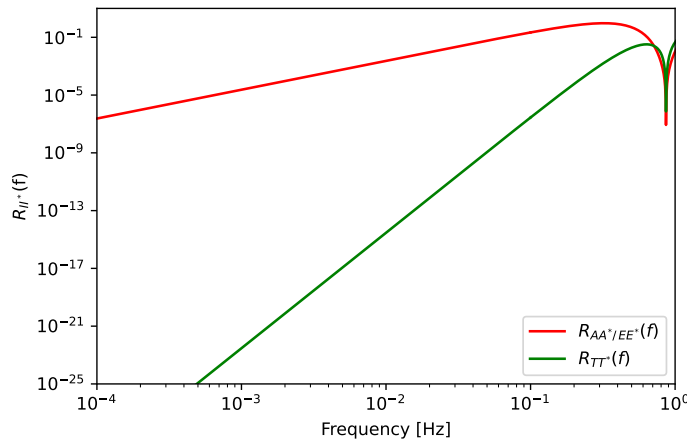


FIG. 2: Analytic average response function for each channel. Compared with the A/E channel, the response of the T channel to GWs is relatively negligible at low frequencies.

The analytic response function for each channel are shown in Fig. 2. Compared with the A/E channel, the response of the T channel is negligible for frequencies below the characteristic frequency ($f_*^{\text{TQ}} \approx 0.28$ Hz), but needs to be considered at high frequencies.

IV. SEARCH METHOD AND RESULTS

A. Bayesian inference

The framework of Bayesian inference is widely used in the community of astronomy, which formulates way to assess the probability distribution $p(\vec{\theta}|D)$ over parameter space $\vec{\theta}$ with the observed data D . The core of Bayesian inference is the Bayes' theorem,

$$p(\vec{\theta}|D) = \frac{\mathcal{L}(\vec{\theta}|D) p(\vec{\theta})}{p(D)}, \quad (21)$$

where $p(\vec{\theta}|D)$, $\mathcal{L}(\vec{\theta}|D) = p(D|\vec{\theta})$, $p(\vec{\theta})$, and $p(D) = \int \mathcal{L}(\vec{\theta}|D) p(\vec{\theta}) d\vec{\theta}$ are posterior, likelihood, prior, and evidence, respectively. The evidence plays a role of normalizing the posterior over parameter space.

Despite the relatively simple expression, it is not straightforward to map the posterior distribution over parameter space efficiently. In practice, stochastic sampling methods like MCMC have been widely adopted to numerically approximate the posterior distribution. Brute force methods like grid-based search suffers from the ‘‘curse of dimensionality’’, while MCMC can efficiently sample in high-dimensional parameter space. Unlike brute force methods, once tuned, the MCMC methods can efficiently sample the parameter space, therefore we adopt the MCMC to obtain the posterior distribution. Specifically, we choose the popular implementation of the affine invariant ensemble sampler, `emcee` [120] for this work.

In addition to the posterior distribution, one also face the problem of model selection, or to identify which model is better supported by the observed data. This is usually done by calculating the *odds ratio* $\frac{p(\mathcal{M}_1|D)}{p(\mathcal{M}_0|D)}$ between the models \mathcal{M}_1 and \mathcal{M}_0 . We observe

$$\frac{p(\mathcal{M}_1|D)}{p(\mathcal{M}_0|D)} = \frac{p(D|\mathcal{M}_1) p(\mathcal{M}_1)}{p(D|\mathcal{M}_0) p(\mathcal{M}_0)}, \quad (22)$$

which states that the odds ratio can be expressed as the product of the *Bayes factor* $\frac{p(D|\mathcal{M}_1)}{p(D|\mathcal{M}_0)}$ and the *prior odds* $\frac{p(\mathcal{M}_1)}{p(\mathcal{M}_0)}$. We set the prior odds to unit so that the data can dominate, and therefore we focus on the Bayes factor for the remaining of the work. The calculation of Bayes factor is enabled through calculating of evidence under both models using the nested sampling (NS) algorithm `dynesty` [121]

Throughout this work, we set the prior on the spectral index to be uniform, and the prior on other parameters to be logarithmically uniform, such as $\log_{10} \Omega_{\text{PL}} \in \mathcal{U}[-15, -9]$, $\log_{10} S_{ij}^a \in \mathcal{U}[-43, -39]$, $\log_{10} S_{ij}^p \in \mathcal{U}[-53, -48]$.

B. Likelihood

For a stationary and Gaussian noise, the likelihood function can be expressed as [2, 53]

$$\mathcal{L}(\vec{\theta}|D) = \prod_k \frac{1}{\sqrt{(2\pi)^3 |C(f_k)|}} \exp \left\{ -\frac{1}{2} D [C(f_k)]^{-1} D^\dagger \right\}, \quad (23)$$

where $D = [A(f_k), E(f_k), T(f_k)]$ is the frequency-domain strain data stream from the three channels, \dagger represents conjugate transpose, $\vec{\theta} \rightarrow \{S_{ij}^a, S_{ij}^p, \Omega_\alpha, \alpha, \Delta\}$ represents our model parameters, and the $\vec{\theta}$ -dependant 3×3 covariance matrix $C(f_k)$ is

$$C(f_k) = \frac{\mathbf{T}_{\text{tot}}}{4} \begin{pmatrix} \langle AA^* \rangle & \langle AE^* \rangle & \langle AT^* \rangle \\ \langle EA^* \rangle & \langle EE^* \rangle & \langle ET^* \rangle \\ \langle TA^* \rangle & \langle TE^* \rangle & \langle TT^* \rangle \end{pmatrix}, \quad (24)$$

includes contributions from both the instrumental noise spectral densities and signal spectral densities.

C. Data simulation

In our simulations, we focus on a simplified scenario and work under the following assumptions:

- (1) Our data are the sum of a SGWB and instrumental noise, i.e., we are working with ideal case, that all resolvable sources, glitches, and any other disturbances have been subtracted perfectly from the data.
- (2) The noise and the signal are Gaussian, stationary, and uncorrelated in frequency domain. Twelve noise components in the cross spectra are described by a model whose parameter values are known to within about $\pm 20\%$ of its nominal values.

The injected values of the SGWB model parameters can be found in Sec. II, and the injected instrumental noise parameters are listed in the second column of Table I.

For the sake of convenience, we generate data directly in the frequency domain, since this allows us to ignore window effects and overlapping segments. We generate a three-month data set at 5 second sampling interval, which is related by a maximum frequency of 0.1 Hz. The correlated noise are generated by

$$\begin{aligned} n_A(f_k) &= \frac{\sqrt{\langle N_{AA^*} \rangle}}{2} (x_1 + i y_1), \\ n_E(f_k) &= c_1 n_A(f_k) + c_2 (x_2 + i y_2), \\ n_T(f_k) &= c_3 n_A(f_k) + c_4 n_E(f_k) + c_5 (x_3 + i y_3). \end{aligned} \quad (25)$$

Likewise, independent signals for each channel can therefore be generated by

$$\begin{aligned} h_A(f_k) &= \frac{\sqrt{S_h(f_k) R_{AA^*}(f_k)}}{2} (x_4 + i y_4), \\ h_E(f_k) &= \frac{\sqrt{S_h(f_k) R_{EE^*}(f_k)}}{2} (x_5 + i y_5), \\ h_T(f_k) &= \frac{\sqrt{S_h(f_k) R_{TT^*}(f_k)}}{2} (x_6 + i y_6). \end{aligned} \quad (26)$$

Here, x_i and y_i , $i = \{1, 2, 3, 4, 5, 6\}$, are statistically-independent real Gaussian random variables, each of zero mean and unit variance, and the coefficients $\{c_1, c_2, c_3, c_4\}$ are derived in the Appendix B.

D. Parameter estimation

The formalism of Eq. (23) means that we can assess the noise parameters from the data. In this subsection, we use TQSGWB to perform Bayesian inference on the GW data under various models, and discuss the ability of assessing the position noise S_{ij}^p and acceleration noise S_{ij}^a . We first investigate the scenario where the data is composed with noise only.

From Eqs. (14), for the instrument noises, one has

$$\begin{aligned} S_{ij}^{a,p} + S_{ji}^{a,p} &= \left(N_{ij}^{a,p} + N_{ji}^{a,p} \right) \\ &\times \begin{cases} \frac{\text{m}^2}{\text{Hz}} \left(\frac{1}{2L} \right)^2 & \text{for p,} \\ \frac{\text{m}^2}{\text{Hz}} \left(1 + \frac{0.1\text{mHz}}{f} \right) \left(\frac{1}{2\pi f} \right)^4 \left(\frac{1}{2L} \right)^2 & \text{for a,} \end{cases} \end{aligned} \quad (27)$$

where the index a, p represent acceleration and position noise, and $N_{ij}^{a,p}$ are the noise amplitude parameters of different arms. Then we can define several new parameters with the sum and difference of noise parameters for each arm, i.e.,

$$M_{ij}^{a,p} = N_{ij}^{a,p} + N_{ji}^{a,p}, \quad (28)$$

$$D_{ij}^{a,p} = N_{ij}^{a,p} - N_{ji}^{a,p}, \quad (29)$$

and the ratio between the differences and the summations

$$R_{ij}^{a,p} = \frac{D_{ij}^{a,p}}{M_{ij}^{a,p}} = \frac{N_{ij}^{a,p} - N_{ji}^{a,p}}{N_{ij}^{a,p} + N_{ji}^{a,p}}. \quad (30)$$

1. Constraint results on the instrument noise only

In this scenario, we compare parameter estimation results under two different covariance matrix: with and without the imaginary components. The contour plots of posterior for the parameters of

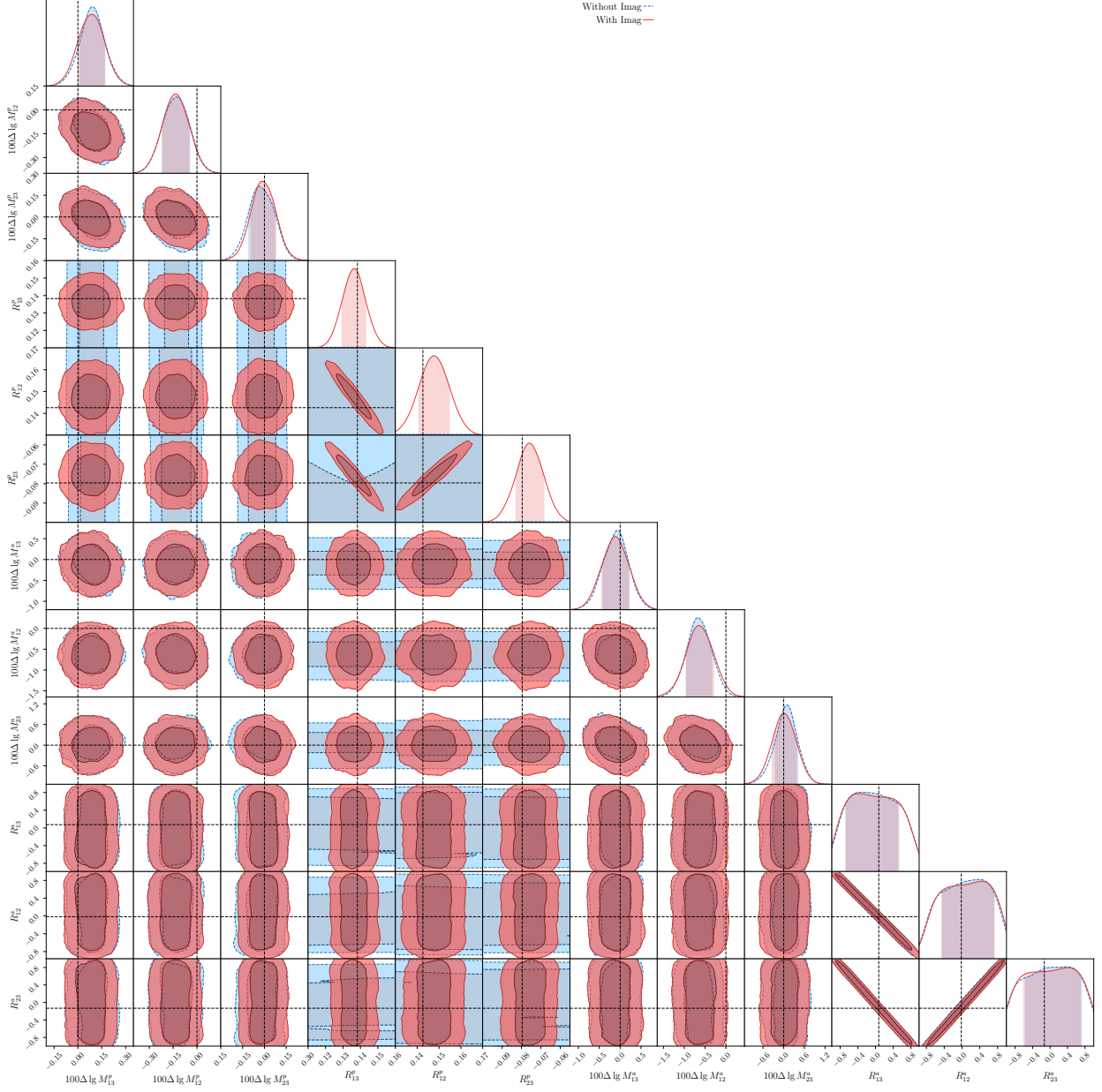


FIG. 3: Corner plots of the noise-only data for the single TianQin configuration. The red (blue) contours and solid (dashed) lines are for the model with (without) imaginary components. The results are for the twelve TianQin noise parameters. The vertical dashed lines represent the injected values of the sum and ratio of six position noises and six acceleration parameters, while the vertical shaded region on the posterior distribution denote 68% credible region, the contour lines denote [68% , 95%] credible regions.

$\Delta \lg M_{ij}^{a,p} = \lg M_{ij}^{a,p} - \lg M_{ij,\text{injected}}^{a,p}$ and $R_{ij}^{a,p}$ are shown in Fig. 3¹. Here, $\lg M_{ij,\text{injected}}^{a,p}$ is the value derived from the injected values, i.e., see Table I. The injected values with dashed lines are also

¹ The contour plots are generated using the plotting utilities `ChainConsumer` [122].

shown in the figures, and also the 68% and 95% credible regions with contour lines. One should note that the simulated data are generated under the covariance with imaginary part, but two different models (with and without) are considered. The contours in blue and dashed lines are for the case without imaginary components, the red contours and solid lines are for the case with imaginary part. And the constraint results of different cases are listed in Table I.

TABLE I: The injected values and constraint results for noise parameters.

Parameter	Injected	Without image	With image
$100\Delta \lg M_{13}^p$	0	$0.091^{+0.079}_{-0.078}$	$0.089^{+0.078}_{-0.088}$
$100\Delta \lg M_{12}^p$	0	$-0.127^{+0.082}_{-0.090}$	$-0.134^{+0.084}_{-0.084}$
$100\Delta \lg M_{23}^p$	0	$-0.035^{+0.107}_{-0.074}$	$-0.016^{+0.094}_{-0.076}$
R_{13}^p	0.1382	–	$0.1365^{+0.0065}_{-0.0070}$
R_{12}^p	0.1426	–	$0.1478^{+0.007}_{-0.007}$
R_{23}^p	-0.0796	–	$-0.0758^{+0.0074}_{-0.0070}$
$100\Delta \lg M_{13}^a$	0	$-0.06^{+0.27}_{-0.35}$	$-0.12^{+0.33}_{-0.33}$
$100\Delta \lg M_{12}^a$	0	$-0.67^{+0.33}_{-0.27}$	$-0.65^{+0.35}_{-0.31}$
$100\Delta \lg M_{23}^a$	0	$0.10^{+0.31}_{-0.34}$	$0.00^{+0.37}_{-0.34}$
R_{13}^a	0.0735	$-0.32^{+0.83}_{-0.35}$	$-0.37^{+0.90}_{-0.30}$
R_{12}^a	-0.0160	$0.38^{+0.34}_{-0.82}$	$0.44^{+0.28}_{-0.89}$
R_{23}^a	-0.1318	$0.38^{+0.35}_{-0.94}$	$0.40^{+0.30}_{-1.00}$
$\lg N_{13}^p$	-23.9272	$-23.85^{+0.12}_{-0.44}$	$-23.93^{+0.0025}_{-0.0029}$
$\lg N_{12}^p$	-23.9439	$-23.89^{+0.15}_{-0.38}$	$-23.94^{+0.0028}_{-0.0027}$
$\lg N_{23}^p$	-24.0485	$-23.88^{+0.10}_{-0.43}$	$-24.05^{+0.0036}_{-0.0035}$
$\lg N_{31}^p$	-24.0481	$-23.86^{+0.11}_{-0.50}$	$-24.05^{+0.0037}_{-0.0034}$
$\lg N_{21}^p$	-24.0687	$-23.91^{+0.16}_{-0.40}$	$-24.07^{+0.0036}_{-0.0038}$
$\lg N_{32}^p$	-23.9792	$-23.89^{+0.13}_{-0.46}$	$-23.98^{+0.0031}_{-0.0029}$
$\lg N_{13}^a$	-29.9284	$-29.85^{+0.16}_{-0.38}$	$-29.86^{+0.16}_{-0.38}$
$\lg N_{12}^a$	-29.9574	$-29.81^{+0.14}_{-0.32}$	$-29.80^{+0.12}_{-0.33}$
$\lg N_{23}^a$	-30.0751	$-29.90^{+0.15}_{-0.40}$	$-29.89^{+0.13}_{-0.41}$
$\lg N_{31}^a$	-29.9924	$-29.83^{+0.15}_{-0.34}$	$-29.82^{+0.13}_{-0.35}$
$\lg N_{21}^a$	-29.9435	$-29.88^{+0.17}_{-0.39}$	$-29.87^{+0.16}_{-0.42}$
$\lg N_{32}^a$	-29.9599	$-29.90^{+0.15}_{-0.42}$	$-29.91^{+0.14}_{-0.42}$

In the table, the symbols “–” represent that the parameters can not be constrained.

For the case of the model without imaginary part. As expected, all summation parameters $M_{ij}^{a,p}$ are well-constrained, with slight negative correlation between different summations. The

latter can be explained by the expression in Appendix A, which shows that for the diagonal terms (for both the position noises and the acceleration noises) all $M_{ij}^{a,p}$ adds up, leading to a negative correlation in between. On the other hand, the ratio parameters $R_{ij}^{a,p}$ are much less constrained, which indicates that the differences parameters $D_{ij}^{a,p}$ are also less constrained. Combining Figs. 3, 4 and Table I, one can find that though the constraint results for all $M_{ij}^{a,p}$ are better, except for the single parameters of $N_{ij}^{a,p}$, the credible regions are much larger than $M_{ij}^{a,p}$. As shown in Fig. 4, there are big biases for the single noise parameters N_{ij}^p , which indicates that, in such case, it is only possible to constrain a certain combination of the noise parameters.

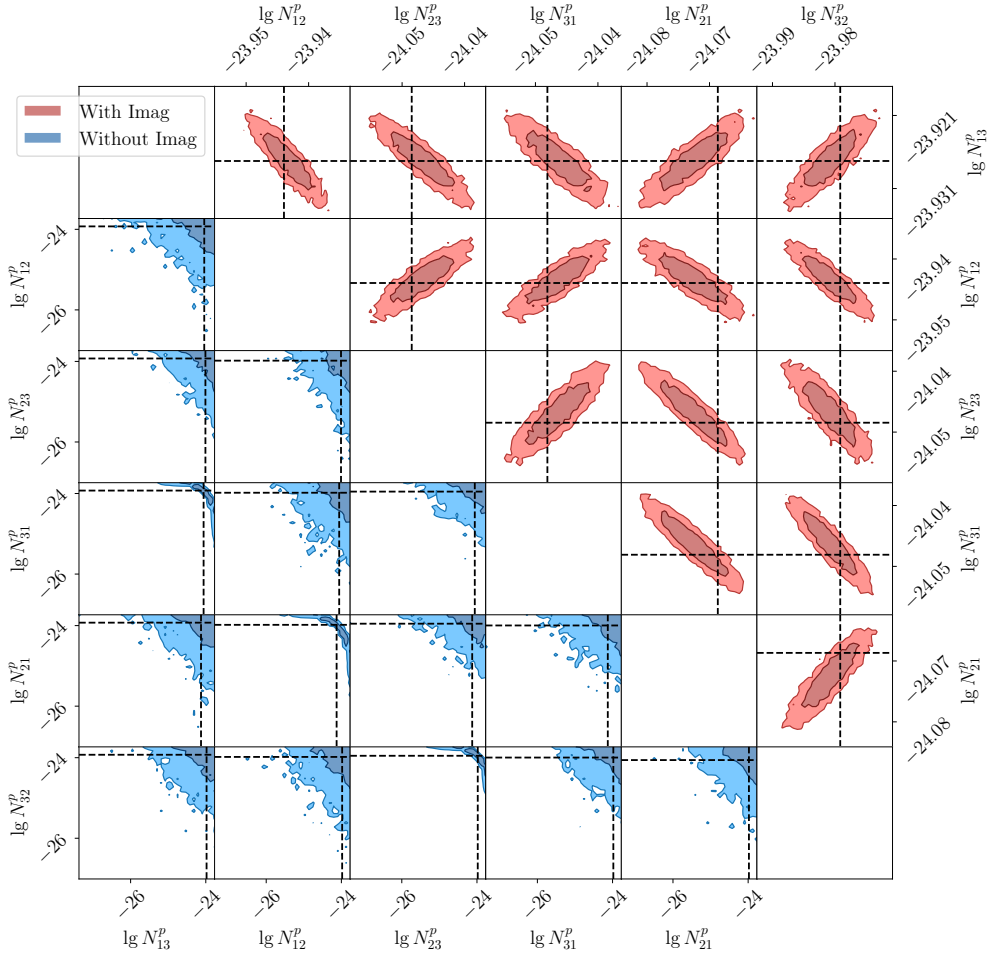


FIG. 4: Contour plots of the six TianQin position noise parameters. The shaded area denote the 68% and 95% credible regions. The dashed line represent the injected values.

Once the imaginary components are included in the calculation, the degeneracies in position noises can be broken. In Fig. 4, we present the position noise parameters N_{ij}^p *per se*. The panels in the upper-right triangle and lower-left triangle are for the contour plots of model with and without

imaginary combinations, respectively. As expected, each pair of position noises are negatively correlated, while correlation exist for other combinations. And for the model without imaginary part, it is straightforward to see that only the contours of paired position noise parameters can be constrained. However, for the model with imaginary part, all the position noise parameters are constrained tightly.

From Fig. 3 and Table I, we observe that the 68% credible region for the summation $M_{ij}^{a,p}$ is similar between models with or without imaginary components. For the ratio parameters, covariance with imaginary components can give a good constraint on R_{ij}^p . While the pattern of the contours remain roughly the same for R_{ij}^a , which is due to that there is no imaginary correlation contribute to the acceleration noise parameters. From Table I and Fig. 4, one can find that the 68% credible region for the summation $\lg N_{ij}^a$ is larger than 0.1 without the imaginary correction, but shrinks to 0.003 with the imaginary correction. This indicates that the credible region for the summation parameters are reduced by two orders of magnitude when the imaginary part is considered.

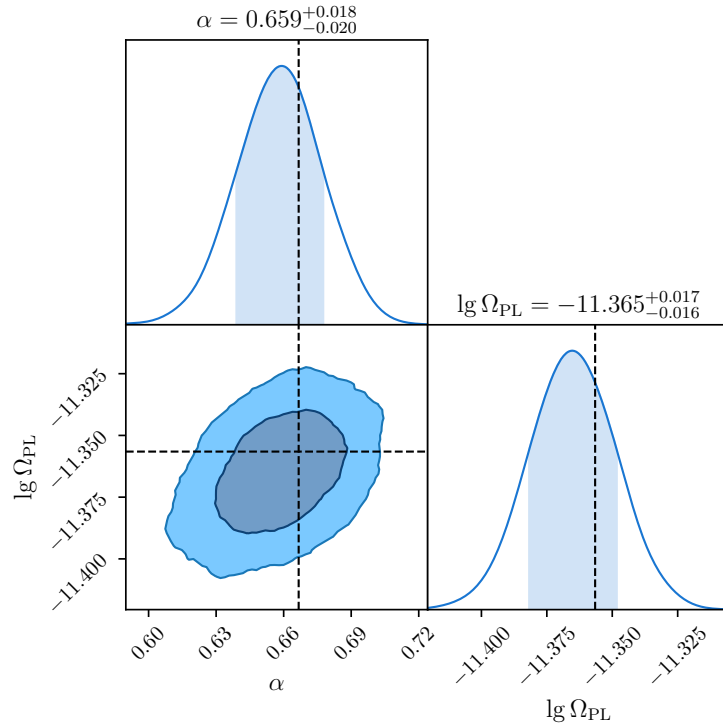


FIG. 5: Corner plots for the noise + power-law SGWB case. Here only the parameters of the SGWB model are shown. The dashed lines represent the injected values.

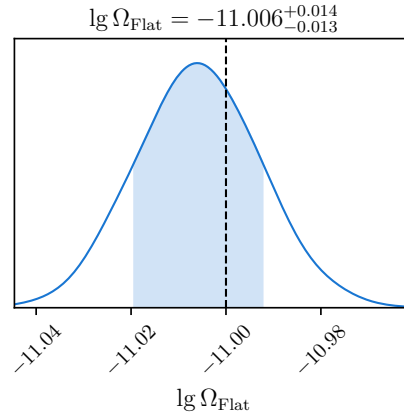


FIG. 6: Posterior distribution of $\lg \Omega_{\text{Flat}}$ for the noise + flat SGWB case. The vertical dashed line represents the injected value.

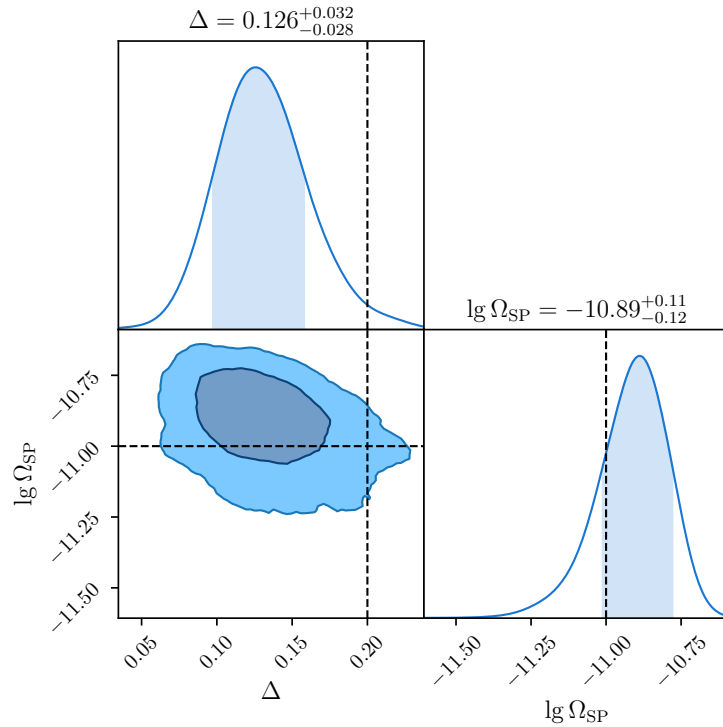


FIG. 7: Corner plots for the noise + SP SGWB case. Here only the parameters of the SGWB model are shown. The dashed lines represent the injected values.

2. Constraint results for different SGWB models

We then turn to the scenarios when SGWB is present in the data. Since A , E , and T channels have uncorrelated responses in the equal arm-length limit, diagonal elements in the covariance matrix, which contain signal and noise components, are used to distinguish SGWB from instrument

noise, while off-diagonal terms are used to increase the constraint on the acceleration noise and position noise. Similar to the noise-only scenario, by adopting the correct model, the injected noise parameters can be recovered precisely.

The constraint results for the parameters of the three SGWB models are shown in Figs. 5, 6, and 7, respectively. Furthermore, the SGWB parameters are also correctly recovered. This results show the encouraging potential of our method to recover noise parameters like N_{ij}^p and N_{ij}^a , as well as the SGWB parameters like α , and Ω . For the power-law SGWB model, the constraint precision of the amplitude parameter can reach the level of $\sim 0.2\%$, while for the index it can reach $\sim 3\%$. For the flat SGWB model, the constraint precision of the amplitude parameter can approach $\sim 0.1\%$. However, for the Gaussian-bump case, the injected value of the parameter Δ lies slightly outside the 68% credible interval. The constraint precisions for Ω_{SP} and Δ reach the level of $\sim 1\%$ and $\sim 25\%$, respectively. This can be partially explained by the low signal-to-noise ratio (SNR) for the injected SGWB.

We present contour plots between the SGWB model parameters and the instrumental noise parameters for a power-law, a flat, and a Gaussian-bump SGWB, respectively in Figs. 9 to 11. From these contour plots, one can find that, though the number of model parameters have been increased, the precision and the biases of the constraint results for the instrument noises are basically unchanged.

E. Detection limit

We then shift attention to the Bayesian model selection. In this part, we aim to answer to which level can we confidently use TQSGWB to identify the existence of SGWB. We consider two models:

- i. \mathcal{M}_0 : data is described by instrument noise only,
- ii. \mathcal{M}_1 : data consists of instrument noise and an SGWB.

To compare the two models, we use the odds ratio, which numerically equals to the Bayes factor when we set the prior odds to be unit

$$\mathcal{B}_0^1 = \frac{\int d\vec{\theta} \mathcal{L}(\vec{\theta}|D, \mathcal{M}_1) p(\vec{\theta}|\mathcal{M}_1)}{\int d\vec{\theta} \mathcal{L}(\vec{\theta}|D, \mathcal{M}_0) p(\vec{\theta}|\mathcal{M}_0)}, \quad (31)$$

where $p(\vec{\theta}|\mathcal{M})$ and the integrand $\mathcal{L}(\vec{\theta}|D, \mathcal{M})$ respectively represent the prior probability and likelihood under the corresponding model.

A positive log Bayes factor $\log \mathcal{B}_0^1$ shows support for the \mathcal{M}_1 over \mathcal{M}_0 . But to avoid the influence from random fluctuation, it is widely suggested that a value of $\log \mathcal{B}_0^1 > 1$ is required for a meaningful followup discussion, and a value of $\log \mathcal{B}_0^1 > 3$ is needed for a strong support of the \mathcal{M}_1 [123].

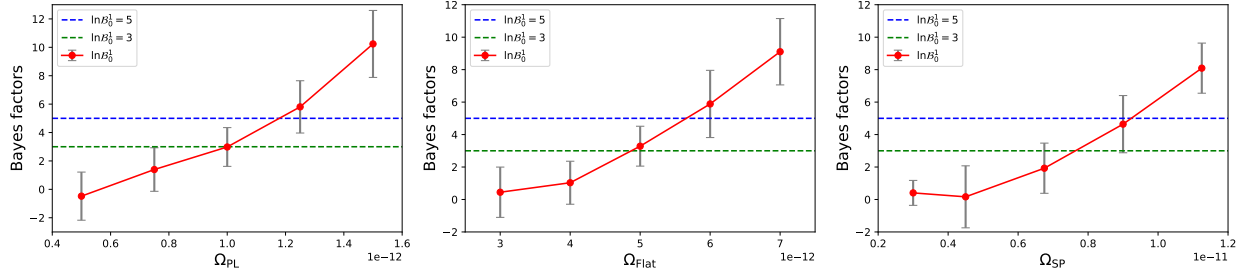


FIG. 8: The Bayes factor as a function of background amplitude Ω_0 in A , E , and T channel, which showing the detectability versus level of a flat background (left plane), a power law background (center plane) and a single-peak background (right plane). The green and blue dotted lines represent the log-Bayes factors 1 and 3, respectively. The magenta line represents the Bayes factor.

In Fig. 8, we present log Bayes factor between the SGWB models and the noise model, with the corresponding SGWB injected in the data, and a total observation period of three months is assumed. In each panel there are multiple horizontal lines, the green dashed line represents a log Bayes factor of 3, and the blue dashed line represents a log Bayes factor of 5.

Our detection confidence becomes very strong (a log Bayes factor of 5) for a power-law background level $\Omega_{PL} = 1.3 \times 10^{-12}$, a flat background level of $\Omega_{Flat} = 6.0 \times 10^{-12}$, and a single-peak background level $\Omega_{SP} = 9.0 \times 10^{-12}$ with three-month data. The corresponding SNRs are around 5, 13, and 8, respectively.

V. SUMMARY AND DISCUSSION

In this paper, we investigated the capability of TianQin to detect various isotropic SGWB using the Bayes analysis method, where a full covariance matrix or cross-correlation between different detection channels is considered in the likelihood function. To the best of the authors' knowledge, for the first time, we include the imaginary components in the cross spectral TDI channels covariance matrix, which raised due to the asymmetrical instrument noises. We perform a Bayesian inference under a number of different cases to demonstrate the validity of the updated covariance matrix. We also applied a model selection analysis to show how sensitive is TianQin to the strength of SGWB model. Three models are considered for the SGWB spectrum: the CBCs (power-law), a

scale invariant inflationary SGWB (flat), and a single-peak spectrum (Gaussian-bump). Throughout our analysis, we have assumed the SGWB and noise to be Gaussian and stationary, and we assume an operation time of three months due to TianQin’s (3+3)-operational model.

We have calculated the cross spectral density of instrumental noise working in the TDI-1.5 channels A , E , and T . Applying the MCMC on noise-only data, we demonstrated that including the imaginary components can help to break degeneracies between different noise parameters, especially for the position noise. Similar conclusions are also observed when three representative SGWB are injected, which demonstrated that both the noise and SGWB parameters can be recovered precisely under the our model.

To assess the detection limit of TianQin to SGWB, we apply Bayesian model selection to noise and SGWB model versus the noise only model. We compute the Bayes factors under different SGWB strengths, and concluded that TianQin will be able to detect the energy density of a PL signal as low as $\Omega_{\text{PL}} = 1.3 \times 10^{-12}$, a flat signal as low as $\Omega_{\text{Flat}} = 6.0 \times 10^{-12}$, and a SP signal as low as $\Omega_{\text{SP}} = 9.0 \times 10^{-12}$ with three-month observation.

The primary purpose of this paper is to explore the detection capability of the SGWB via TianQin, and focusing on the impacts of including the imaginary component of the covariance matrix. What is more, the discussion here focuses on distinguishing single-component SGWB from instrument noise, and does not yet address issues of identifying astrophysical and cosmological sources simultaneously.

One line of our future study is to extend to multiple independent space-based GW detectors, such as TianQin-LISA network. TianQin and LISA are two mHz band space-based GW detectors which will probably fly at roughly the same time, around 2035. With this network, one can expect to apply the cross-correlation method to detect SGWB. Another line is to see how the limit is affected by astrophysical confusion foregrounds, such as the noise from un-resolved white dwarf binaries in our Galaxy. We leave those for future works.

Acknowledgments

The authors would like to thank Pan-Pan Wang for discussing response function and Zhiyuan Li for useful conversations. This work has been supported by the National Key Research and Development Program of China (Grant No. 2020YFC2201400), the Guangdong Major Project of Basic and Applied Basic Research (Grant No. 2019B030302001), the Natural Science Foundation of China (Grant No. 12173104), the fellowship of China Postdoctoral Science Foundation

(Grant No. 2021M703769), and the Natural Science Foundation of Guangdong Province of China (Grant No. 2022A1515011862). We acknowledge the support by National Supercomputer Center in Guangzhou.

Appendix A: Cross spectra

Here we provide a detailed calculation with respect to the noise cross spectra between different TDI channels.

Due to the absence of correlation between different links as well as types of noise, the one-sided Gaussian spectral density of the noise can be defined as [124]

$$\langle \tilde{n}_{ij}^\alpha(f) \tilde{n}_{kl}^{\beta*}(f') \rangle = \frac{1}{2} \delta_{ij,kl} \delta_{\alpha,\beta} \delta(f-f') S_{ij}^\alpha(f), \quad (\text{A1})$$

where α and β are employed to label the position noise and the acceleration noise. Based on the construction of the *AET* channel group (i.e., Eq. (12)), the noise cross spectra are given by

$$\begin{aligned} \langle N_{AA^*}^p \rangle &= 2 \sin^2 u \left\{ 2[1 + \cos u] (S_{13}^p + S_{31}^p) + (S_{12}^p + S_{21}^p) + (S_{23}^p + S_{32}^p) \right\} \\ \langle N_{AA^*}^a \rangle &= 8 \sin^2 u \left\{ [1 + \cos u]^2 (S_{13}^a + S_{31}^a) + \cos^2 u (S_{21}^a + S_{23}^a) + (S_{12}^a + S_{32}^a) \right\} \\ \langle N_{EE^*}^p \rangle &= \frac{2}{3} \sin^2 u \left\{ 2[1 - \cos u] (S_{13}^p + S_{31}^p) + [5 + 4 \cos u] (S_{12}^p + S_{21}^p + S_{23}^p + S_{32}^p) \right\} \\ \langle N_{EE^*}^a \rangle &= \frac{8}{3} \sin^2 u \left\{ [1 + 2 \cos^2 u]^2 (S_{12}^a + S_{32}^a) + [2 + \cos^2 u]^2 (S_{21}^a + S_{23}^a) + [1 - \cos u]^2 (S_{13}^a + S_{31}^a) \right\} \\ \langle N_{TT^*}^p \rangle &= \frac{16}{3} \sin^2 u \sin^2 \left(\frac{u}{2} \right) (S_{12}^p + S_{21}^p + S_{13}^p + S_{31}^p + S_{23}^p + S_{32}^p) \\ \langle N_{TT^*}^a \rangle &= \frac{64}{3} \sin^2 u \sin^4 \left(\frac{u}{2} \right) (S_{12}^a + S_{21}^a + S_{13}^a + S_{31}^a + S_{23}^a + S_{32}^a) \\ \langle N_{AE^*}^p \rangle &= \frac{2}{\sqrt{3}} \sin^2 u \left\{ [1 + 2 \cos u] (S_{23}^p + S_{32}^p - S_{12}^p - S_{21}^p) + i 2 \sin u (S_{12}^p - S_{21}^p - S_{13}^p + S_{31}^p + S_{23}^p - S_{32}^p) \right\} \\ \langle N_{AE^*}^a \rangle &= \frac{8}{\sqrt{3}} \sin^2 u \left\{ \sin^2 u (S_{31}^a - S_{13}^a) + \cos u [2 + \cos u] (S_{23}^a - S_{21}^a) + [1 + 2 \cos u] (S_{32}^a - S_{12}^a) \right\} \\ \langle N_{AT^*}^p \rangle &= 2 \sqrt{\frac{2}{3}} \sin^2 u \left\{ [1 - \cos u] (S_{23}^p + S_{32}^p - S_{12}^p - S_{21}^p) - i \sin u (S_{12}^p - S_{21}^p + S_{23}^p - S_{32}^p + 2S_{13}^p - 2S_{31}^p) \right\} \\ \langle N_{AT^*}^a \rangle &= 8 \sqrt{\frac{2}{3}} \sin^2 u \left\{ \sin^2 u (S_{13}^a - S_{31}^a) + \cos u [\cos u - 1] (S_{23}^a - S_{21}^a) + 2[\cos u - 2] (S_{12}^a - S_{32}^a) \right\} \\ \langle N_{ET^*}^p \rangle &= \frac{2\sqrt{2}}{3} \sin^2 u \left\{ [1 - \cos u] (2S_{13}^p + 2S_{31}^p - S_{21}^p - S_{12}^p - S_{23}^p - S_{32}^p) - i 3 \sin u (S_{21}^p - S_{12}^p + S_{23}^p - S_{32}^p) \right\} \\ \langle N_{ET^*}^a \rangle &= \frac{8\sqrt{2}}{3} \sin^2 u [\cos u - 1] \left\{ [\cos u - 1] (S_{13}^a + S_{31}^a) + [\cos u + 2] (S_{21}^a + S_{23}^a) + [2 \cos u + 1] (S_{12}^a + S_{32}^a) \right\} \end{aligned} \quad (\text{A2})$$

According to the above equations, if we assume symmetry between instrumental noises, then we can safely ignore imaginary terms, However, once we abandon the symmetric assumption, one can find that it is no longer safe to ignore the imaginary part. Take $\langle N_{AT^*}^p \rangle$ and $\langle N_{ET^*}^p \rangle$ for example, the imaginary part is of the order $\sim u$, while the real part is of the order $(1 - \cos u)$, so in the low frequency limit, the imaginary terms have a higher impact than the real terms.

Assuming that the three arm-lengths are equal and the noise in each satellite is exactly identical, the corresponding channel noise power spectral density can be analytically expressed as

$$\begin{aligned} \langle N_{AA} \rangle = \langle N_{EE} \rangle &= 8 \sin^2 u \left\{ [2 + \cos u] S^p + 4 [1 + \cos u + \cos^2 u] S^a \right\}, \\ \langle N_{TT} \rangle &= 16 \sin^2 u \left\{ [1 - \cos u] S^p + 2 [1 - \cos u]^2 S^a \right\}. \end{aligned} \quad (\text{A3})$$

Appendix B: Data generation

We derive in detail here the values of the coefficients that enter expressions (25),

$$\begin{aligned} \langle n_A(f_k) n_E^*(f_k) \rangle &= \langle n_A(f_k) n_A^*(f_k) \rangle c_1^* \equiv \frac{1}{2} \langle N_{AE^*} \rangle, \\ \langle n_E(f_k) n_E^*(f_k) \rangle &= \langle n_A(f_k) n_A^*(f_k) \rangle |c_1|^2 + 2|c_2|^2 \equiv \frac{1}{2} \langle N_{EE^*} \rangle, \\ \Rightarrow c_1 &= \frac{\langle N_{EA^*} \rangle}{\langle N_{AA^*} \rangle}, \quad c_2 = \frac{\sqrt{\langle N_{EE^*} \rangle - \langle N_{AA^*} \rangle} |c_1|^2}{2}. \end{aligned} \quad (\text{B1})$$

Analogously, the parameters for simulating $n_T(f_k)$ are derived

$$\begin{aligned} \langle n_A(f_k) n_T^*(f_k) \rangle &= \langle n_A(f_k) n_A^*(f_k) \rangle c_3^* + \langle n_A(f_k) n_E^*(f_k) \rangle c_4^* \equiv \frac{1}{2} \langle N_{AT^*} \rangle, \\ \langle n_E(f_k) n_T^*(f_k) \rangle &= \langle n_E(f_k) n_A^*(f_k) \rangle c_3^* + \langle n_E(f_k) n_E^*(f_k) \rangle c_4^* \equiv \frac{1}{2} \langle N_{ET^*} \rangle, \\ \langle n_T(f_k) n_T^*(f_k) \rangle &= \langle n_T(f_k) n_A^*(f_k) \rangle c_3^* + \langle n_T(f_k) n_E^*(f_k) \rangle c_4^* + 2|c_5|^2 \equiv \frac{1}{2} \langle N_{TT^*} \rangle, \\ \Rightarrow c_3 &= \sqrt{\frac{\langle N_{TA^*} \rangle \langle N_{EE^*} \rangle - \langle N_{EA^*} \rangle \langle N_{TE^*} \rangle}{\langle N_{AA^*} \rangle \langle N_{EE^*} \rangle - \langle N_{AE^*} \rangle \langle N_{EA^*} \rangle}}, \\ c_4 &= \sqrt{\frac{\langle N_{AA^*} \rangle \langle N_{TE^*} \rangle - \langle N_{TA^*} \rangle \langle N_{AE^*} \rangle}{\langle N_{AA^*} \rangle \langle N_{EE^*} \rangle - \langle N_{AE^*} \rangle \langle N_{EA^*} \rangle}}, \\ c_5 &= \frac{\sqrt{\langle N_{TT^*} \rangle - c_3 \langle N_{AT^*} \rangle - c_4 \langle N_{ET^*} \rangle}}{2}. \end{aligned} \quad (\text{B2})$$

Appendix C: Parameter estimation with different SGWB models

Here we present the parameter estimation results. We inject different types of SGWBs, and recover under the same SGWB models.

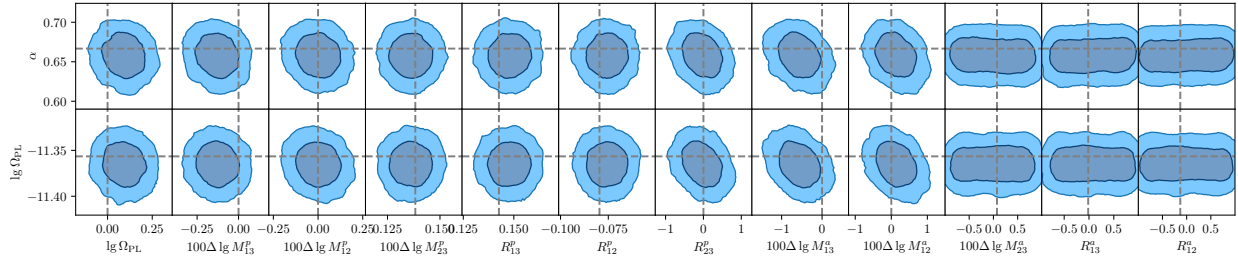


FIG. 9: Contour plot for the noise + power-law SGWB case for single TianQin configuration. The vertical lines represent the injected values of the twelve noise parameters and two SGWB parameters (amplitude and spectral slope), while the vertical dashed lines on the posterior distribution denote from left to right the quantiles [16% , 84%].

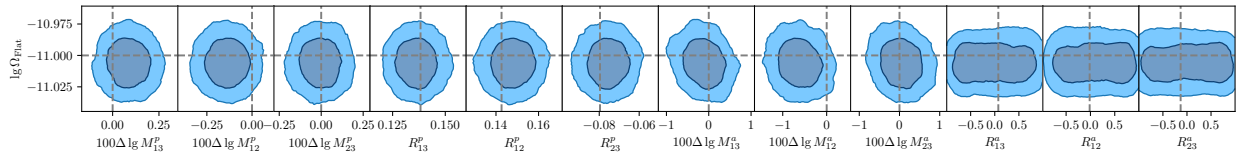


FIG. 10: Contour plot for the noise+flat SGWB case for single TianQin configuration. The vertical line represents the injected values of the 12 noise parameters, while the vertical dashed lines on the posterior distribution denote from left to right the quantiles [16% , 84%].

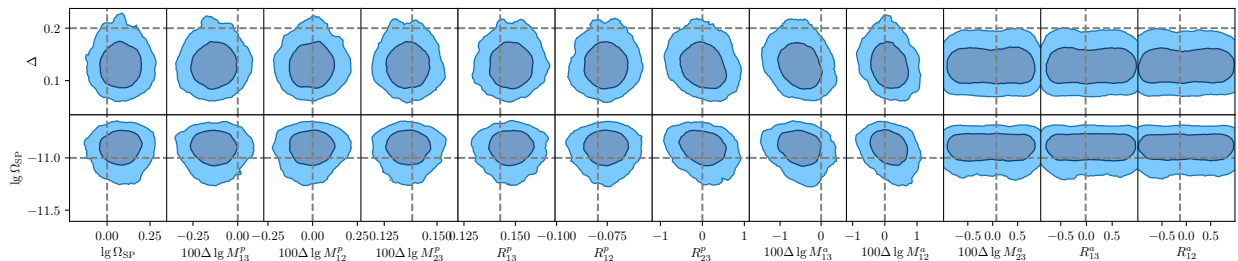


FIG. 11: Contour plot for the noise+SP SGWB case with single TianQin configuration. The vertical line represents the injected values of the 12 noise parameters, while the vertical dashed lines on the posterior distribution denote from left to right the quantiles [16% , 84%].

-
- [1] B. Allen and J. D. Romano, Phys. Rev. D **59**, 102001 (1999), gr-qc/9710117.
 - [2] J. D. Romano and N. J. Cornish, Living Rev. Rel. **20**, 2 (2017), 1608.06889.
 - [3] N. Christensen, Rept. Prog. Phys. **82**, 016903 (2019), 1811.08797.
 - [4] S.-J. Huang, Y.-M. Hu, V. Korol, P.-C. Li, Z.-C. Liang, Y. Lu, H.-T. Wang, S. Yu, and J. Mei, Phys. Rev. D **102**, 063021 (2020), 2005.07889.

- [5] H.-T. Wang et al., Phys. Rev. D **100**, 043003 (2019), 1902.04423.
- [6] S. Liu, Y.-M. Hu, J.-d. Zhang, and J. Mei, Phys. Rev. D **101**, 103027 (2020), 2004.14242.
- [7] S. Liu, L.-G. Zhu, Y.-M. Hu, J.-d. Zhang, and M.-J. Ji, Phys. Rev. D **105**, 023019 (2022), 2110.05248.
- [8] H.-M. Fan, Y.-M. Hu, E. Barausse, A. Sesana, J.-d. Zhang, X. Zhang, T.-G. Zi, and J. Mei, Phys. Rev. D **102**, 063016 (2020), 2005.08212.
- [9] T.-G. Zi, J.-D. Zhang, H.-M. Fan, X.-T. Zhang, Y.-M. Hu, C. Shi, and J. Mei, Phys. Rev. D **104**, 064008 (2021), 2104.06047.
- [10] N. Mazumder, S. Mitra, and S. Dhurandhar, Phys. Rev. D **89**, 084076 (2014), 1401.5898.
- [11] T. Callister, L. Sammut, S. Qiu, I. Mandel, and E. Thrane, Phys. Rev. X **6**, 031018 (2016), 1604.02513.
- [12] A. Maselli, S. Marassi, V. Ferrari, K. Kokkotas, and R. Schneider, Phys. Rev. Lett. **117**, 091102 (2016), 1606.04996.
- [13] M. Maggiore, ICTP Lect. Notes Ser. **3**, 397 (2001), gr-qc/0008027, URL <https://arxiv.org/abs/gr-qc/0008027>.
- [14] C. Caprini and D. G. Figueroa, Class. Quant. Grav. **35**, 163001 (2018), 1801.04268.
- [15] A. H. Guth and S. Y. Pi, Phys. Rev. Lett. **49**, 1110 (1982).
- [16] N. Bartolo et al., JCAP **12**, 026 (2016), 1610.06481.
- [17] C. J. Hogan, Phys. Lett. B **133**, 172 (1983).
- [18] C. Caprini et al., JCAP **04**, 001 (2016), 1512.06239.
- [19] C. Caprini et al., JCAP **03**, 024 (2020), 1910.13125.
- [20] T. W. B. Kibble, J. Phys. A **9**, 1387 (1976).
- [21] P. Auclair et al., JCAP **04**, 034 (2020), 1909.00819.
- [22] L. Valbusa Dall'Armi, A. Ricciardone, N. Bartolo, D. Bertacca, and S. Matarrese, Phys. Rev. D **103**, 023522 (2021), 2007.01215.
- [23] B. Wang and Y. Zhang, Res. Astron. Astrophys. **19**, 024 (2019), 1808.02995.
- [24] J. Aasi et al. (LIGO Scientific, VIRGO), Class. Quant. Grav. **32**, 115012 (2015), 1410.7764.
- [25] F. Acernese et al. (VIRGO), Class. Quant. Grav. **32**, 024001 (2015), 1408.3978.
- [26] M. Sazhin, Soviet Astronomy **22**, 36 (1978), URL <https://articles.adsabs.harvard.edu/pdf/1978SvA...22...36S>.
- [27] S. L. Detweiler, Astrophys. J. **234**, 1100 (1979).
- [28] R. S. Foster and D. C. Backer, The Astrophysical Journal **361** (1990), URL <https://articles.adsabs.harvard.edu/pdf/1990ApJ...361..300F>.
- [29] M. Punturo et al., Class. Quant. Grav. **27**, 194002 (2010).
- [30] B. P. Abbott et al. (LIGO Scientific), Class. Quant. Grav. **34**, 044001 (2017), 1607.08697.
- [31] D. Reitze et al., Bull. Am. Astron. Soc. **51**, 035 (2019), 1907.04833, URL <https://arxiv.org/abs/1907.04833>.
- [32] P. Amaro-Seoane et al. (LISA) (2017), 1702.00786.
- [33] J. Luo et al. (TianQin), Class. Quant. Grav. **33**, 035010 (2016), 1512.02076.

- [34] R. Abbott et al. (KAGRA, Virgo, LIGO Scientific), *Phys. Rev. D* **104**, 022004 (2021), 2101.12130.
- [35] Z. Arzoumanian et al. (NANOGrav), *Astrophys. J. Lett.* **905**, L34 (2020), 2009.04496.
- [36] B. Goncharov et al., *Astrophys. J. Lett.* **917**, L19 (2021), 2107.12112.
- [37] S. Chen et al., *Mon. Not. Roy. Astron. Soc.* **508**, 4970 (2021), 2110.13184.
- [38] J. Ellis and M. Lewicki, *Phys. Rev. Lett.* **126**, 041304 (2021), 2009.06555.
- [39] A. Addazi, Y.-F. Cai, Q. Gan, A. Marciano, and K. Zeng, *Sci. China Phys. Mech. Astron.* **64**, 290411 (2021), 2009.10327.
- [40] W. Ratzinger and P. Schwaller, *SciPost Phys.* **10**, 047 (2021), 2009.11875.
- [41] S. Blasi, V. Brdar, and K. Schmitz, *Phys. Rev. Lett.* **126**, 041305 (2021), 2009.06607.
- [42] W. Buchmuller, V. Domcke, and K. Schmitz, *Phys. Lett. B* **811**, 135914 (2020), 2009.10649.
- [43] R. Samanta and S. Datta, *JHEP* **05**, 211 (2021), 2009.13452.
- [44] Y. Nakai, M. Suzuki, F. Takahashi, and M. Yamada, *Phys. Lett. B* **816**, 136238 (2021), 2009.09754.
- [45] A. Neronov, A. Roper Pol, C. Caprini, and D. Semikoz, *Phys. Rev. D* **103**, L041302 (2021), 2009.14174.
- [46] Z.-C. Chen, C. Yuan, and Q.-G. Huang, *Sci. China Phys. Mech. Astron.* **64**, 120412 (2021), 2101.06869.
- [47] R. w. Hellings and G. s. Downs, *Astrophys. J. Lett.* **265**, L39 (1983).
- [48] N. Christensen, *Phys. Rev. D* **46**, 5250 (1992).
- [49] E. E. Flanagan, *Phys. Rev. D* **48**, 2389 (1993), astro-ph/9305029.
- [50] N. Seto, *Phys. Rev. Lett.* **125**, 251101 (2020), 2009.02928.
- [51] F. B. Estabrook, M. Tinto, and J. W. Armstrong, *Phys. Rev. D* **62**, 042002 (2000).
- [52] C. J. Hogan and P. L. Bender, *Phys. Rev. D* **64**, 062002 (2001), astro-ph/0104266.
- [53] M. R. Adams and N. J. Cornish, *Phys. Rev. D* **82**, 022002 (2010), 1002.1291.
- [54] M. R. Adams and N. J. Cornish, *Phys. Rev. D* **89**, 022001 (2014), 1307.4116.
- [55] M. Pieroni and E. Barausse, *JCAP* **07**, 021 (2020), [Erratum: *JCAP* 09, E01 (2020)], 2004.01135.
- [56] N. Karnesis, M. Lilley, and A. Petiteau, *Class. Quant. Grav.* **37**, 215017 (2020), 1906.09027.
- [57] C. Caprini, D. G. Figueroa, R. Flauger, G. Nardini, M. Peloso, M. Pieroni, A. Ricciardone, and G. Tasinato, *JCAP* **11**, 017 (2019), 1906.09244.
- [58] R. Flauger, N. Karnesis, G. Nardini, M. Pieroni, A. Ricciardone, and J. Torrado, *JCAP* **01**, 059 (2021), 2009.11845.
- [59] G. Boileau, N. Christensen, R. Meyer, and N. J. Cornish, *Phys. Rev. D* **103**, 103529 (2021), 2111.05055.
- [60] G. Boileau, A. Lamberts, N. J. Cornish, and R. Meyer, *Mon. Not. Roy. Astron. Soc.* **508**, 803 (2021), [Erratum: *Mon. Not. Roy. Astron. Soc.* 508, 5554–5555 (2021)], 2105.04283.
- [61] N. Seto and A. Cooray, *Phys. Rev. D* **70**, 123005 (2004), astro-ph/0403259.
- [62] D. Alonso, G. Cusin, P. G. Ferreira, and C. Pitrou, *Phys. Rev. D* **102**, 023002 (2020), 2002.02888.
- [63] N. Bartolo et al. (LISA Cosmology Working Group) (2022), 2201.08782.
- [64] R. Abbott et al. (KAGRA, Virgo, LIGO Scientific), *Phys. Rev. D* **104**, 022005 (2021), 2103.08520.
- [65] Y.-M. Hu, J. Mei, and J. Luo, *Natl. Sci. Rev.* **4**, 683 (2017), URL <https://academic.oup.com/nsr/article/4/5/683/4653094?login=true>.

- [66] J. Mei et al. (TianQin), PTEP **2021**, 05A107 (2021), 2008.10332.
- [67] P. A. R. Ade et al. (Planck), Astron. Astrophys. **594**, A13 (2016), 1502.01589.
- [68] A. Sesana, Phys. Rev. Lett. **116**, 231102 (2016), 1602.06951.
- [69] B. P. Abbott et al. (LIGO Scientific, Virgo), Phys. Rev. X **9**, 031040 (2019), 1811.12907.
- [70] R. Abbott et al. (LIGO Scientific, Virgo), Phys. Rev. D **102**, 043015 (2020), 2004.08342.
- [71] R. Abbott et al. (LIGO Scientific, Virgo), Astrophys. J. Lett. **896**, L44 (2020), 2006.12611.
- [72] R. Abbott et al. (LIGO Scientific, Virgo), Phys. Rev. Lett. **125**, 101102 (2020), 2009.01075.
- [73] B. P. Abbott et al. (LIGO Scientific, Virgo), Astrophys. J. Lett. **892**, L3 (2020), 2001.01761.
- [74] Z.-C. Liang, Y.-M. Hu, Y. Jiang, J. Cheng, J.-d. Zhang, and J. Mei, Phys. Rev. D **105**, 022001 (2022), 2107.08643.
- [75] B. P. Abbott et al. (LIGO Scientific, Virgo), Phys. Rev. Lett. **120**, 091101 (2018), 1710.05837.
- [76] T. Regimbau, Res. Astron. Astrophys. **11**, 369 (2011), 1101.2762.
- [77] A. J. Farmer and E. S. Phinney, Mon. Not. Roy. Astron. Soc. **346**, 1197 (2003), astro-ph/0304393.
- [78] C. J. Moore, R. H. Cole, and C. P. L. Berry, Class. Quant. Grav. **32**, 015014 (2015), 1408.0740.
- [79] B. P. Abbott et al. (LIGO Scientific, Virgo), Phys. Rev. D **100**, 061101 (2019), 1903.02886.
- [80] Z.-C. Chen, F. Huang, and Q.-G. Huang, Astrophys. J. **871**, 97 (2019), 1809.10360.
- [81] L. P. Grishchuk, Zh. Eksp. Teor. Fiz. **67**, 825 (1974), URL http://www.jetp.ras.ru/cgi-bin/dn/e_040_03_0409.pdf.
- [82] L. P. Grishchuk, Class. Quant. Grav. **10**, 2449 (1993), gr-qc/9302036.
- [83] A. A. Starobinsky, JETP Lett. **30**, 682 (1979), URL http://jetpletters.ru/ps/1370/article_20738.shtml.
- [84] M. Maggiore, Phys. Rept. **331**, 283 (2000), gr-qc/9909001.
- [85] M. Kamionkowski, A. Kosowsky, and M. S. Turner, Phys. Rev. D **49**, 2837 (1994), astro-ph/9310044.
- [86] C. Caprini, R. Durrer, and G. Servant, Phys. Rev. D **77**, 124015 (2008), 0711.2593.
- [87] S. J. Huber and T. Konstandin, JCAP **09**, 022 (2008), 0806.1828.
- [88] M. Hindmarsh, S. J. Huber, K. Rummukainen, and D. J. Weir, Phys. Rev. Lett. **112**, 041301 (2014), 1304.2433.
- [89] M. Hindmarsh, S. J. Huber, K. Rummukainen, and D. J. Weir, Phys. Rev. D **92**, 123009 (2015), 1504.03291.
- [90] R. Namba, M. Peloso, M. Shiraishi, L. Sorbo, and C. Unal, JCAP **01**, 041 (2016), 1509.07521.
- [91] B. Thorne, T. Fujita, M. Hazumi, N. Katayama, E. Komatsu, and M. Shiraishi, Phys. Rev. D **97**, 043506 (2018), 1707.03240.
- [92] C. Shi, J. Bao, H. Wang, J.-d. Zhang, Y. Hu, A. Sesana, E. Barausse, J. Mei, and J. Luo, Phys. Rev. D **100**, 044036 (2019), 1902.08922.
- [93] J. Bao, C. Shi, H. Wang, J.-d. Zhang, Y. Hu, J. Mei, and J. Luo, Phys. Rev. D **100**, 084024 (2019), 1905.11674.
- [94] L.-G. Zhu, Y.-M. Hu, H.-T. Wang, J.-D. Zhang, X.-D. Li, M. Hendry, and J. Mei (2021), 2104.11956.

- [95] L.-G. Zhu, L.-H. Xie, Y.-M. Hu, S. Liu, E.-K. Li, N. R. Napolitano, B.-T. Tang, J.-d. Zhang, and J. Mei (2021), 2110.05224.
- [96] B.-B. Ye, X. Zhang, M.-Y. Zhou, Y. Wang, H.-M. Yuan, D. Gu, Y. Ding, J. Zhang, J. Mei, and J. Luo, *Int. J. Mod. Phys. D* **28**, 1950212 (2019), 2012.03260.
- [97] X. Zhang, C. Luo, L. Jiao, B. Ye, H. Yuan, L. Cai, D. Gu, J. Mei, and J. Luo, *Phys. Rev. D* **103**, 062001 (2021), 2012.03264.
- [98] R. Schilling, *Class. Quant. Grav.* **14**, 1513 (1997).
- [99] N. J. Cornish and S. L. Larson, *Class. Quant. Grav.* **18**, 3473 (2001), gr-qc/0103075.
- [100] N. J. Cornish, *Phys. Rev. D* **65**, 022004 (2002), gr-qc/0106058.
- [101] N. J. Cornish and L. J. Rubbo, *Phys. Rev. D* **67**, 022001 (2003), [Erratum: *Phys.Rev.D* 67, 029905 (2003)], gr-qc/0209011.
- [102] M. Tinto and J. W. Armstrong, *Phys. Rev. D* **59**, 102003 (1999).
- [103] M. Tinto, F. B. Estabrook, and J. W. Armstrong, *Phys. Rev. D* **65**, 082003 (2002).
- [104] T. A. Prince, M. Tinto, S. L. Larson, and J. W. Armstrong, *Phys. Rev. D* **66**, 122002 (2002), gr-qc/0209039.
- [105] M. Tinto and S. V. Dhurandhar, *Living Rev. Rel.* **24**, 1 (2021).
- [106] J.-B. Bayle, M. Lilley, A. Petiteau, and H. Halloin, *Phys. Rev. D* **99**, 084023 (2019), 1811.01575.
- [107] M. Vallisneri, J. Crowder, and M. Tinto, *Class. Quant. Grav.* **25**, 065005 (2008), 0710.4369.
- [108] L. S. Finn, S. L. Larson, and J. D. Romano, *Phys. Rev. D* **79**, 062003 (2009), 0811.3582.
- [109] S. L. Larson, W. A. Hiscock, and R. W. Hellings, *Phys. Rev. D* **62**, 062001 (2000), gr-qc/9909080.
- [110] S. L. Larson, R. W. Hellings, and W. A. Hiscock, *Phys. Rev. D* **66**, 062001 (2002), gr-qc/0206081.
- [111] C. Zhang, Q. Gao, Y. Gong, D. Liang, A. J. Weinstein, and C. Zhang, *Phys. Rev. D* **100**, 064033 (2019), 1906.10901.
- [112] D. Liang, Y. Gong, A. J. Weinstein, C. Zhang, and C. Zhang, *Phys. Rev. D* **99**, 104027 (2019), 1901.09624.
- [113] A. Blaut, *Phys. Rev. D* **85**, 043005 (2012), 1901.11268.
- [114] M. Tinto and M. E. da Silva Alves, *Phys. Rev. D* **82**, 122003 (2010), 1010.1302.
- [115] X.-Y. Lu, Y.-J. Tan, and C.-G. Shao, *Phys. Rev. D* **100**, 044042 (2019), 2007.03400.
- [116] C. Zhang, Q. Gao, Y. Gong, B. Wang, A. J. Weinstein, and C. Zhang, *Phys. Rev. D* **101**, 124027 (2020), 2003.01441.
- [117] P.-P. Wang, Y.-J. Tan, W.-L. Qian, and C.-G. Shao, *Phys. Rev. D* **103**, 063021 (2021).
- [118] P.-P. Wang, Y.-J. Tan, W.-L. Qian, and C.-G. Shao, *Phys. Rev. D* **104**, 023002 (2021).
- [119] P.-P. Wang, W.-L. Qian, Y.-J. Tan, H.-Z. Wu, and C.-G. Shao (2022), 2205.08709.
- [120] D. Foreman-Mackey, D. W. Hogg, D. Lang, and J. Goodman, *Publ. Astron. Soc. Pac.* **125**, 306 (2013), 1202.3665.
- [121] J. S. Speagle, *Mon. Not. Roy. Astron. Soc.* **493**, 3132 (2020), 1904.02180.
- [122] S. R. Hinton, *The Journal of Open Source Software* **1**, 00045 (2016).

- [123] R. E. Kass and A. E. Raftery, *J. Am. Statist. Assoc.* **90**, 773 (1995).
- [124] M. Vallisneri and C. R. Galley, *Class. Quant. Grav.* **29**, 124015 (2012), 1201.3684.